

AO-assisted observations of G61.48+0.09^{*,**}

Massive star formation at high resolution

E. Puga¹, C. Alvarez¹, M. Feldt¹, Th. Henning¹, and S. Wolf²

¹ Max-Planck-Institut für Astronomie, Königstuhl 17, 69117 Heidelberg, Germany
e-mail: puga@mpia-hd.mpg.de

² California Institute of Technology, 1201 East California Blvd, MS 105-24 Pasadena, CA 91125, USA

Received 24 November 2003 / Accepted 7 June 2004

Abstract. The characterisation of the stellar populations of ultra-compact HII (UCHII) regions is one of the key means of understanding the formation and evolution of massive stars. Adaptive Optics (AO) assisted near-infrared (NIR) observations provide sufficient resolution and sensitivity to detect such populations at moderate extinction values. We present NIR high-resolution observations of G61.48+0.09, a morphologically complex UCHII region with two components, whose accessible stellar content in the NIR has been widely studied before. A polarimetric map in the K' band, as well as $H_2(1-0) S(1)$ and Bry narrow-band images of the region have been obtained with the AO system ALFA at the Calar Alto Observatory's 3.5 m telescope. We also present high-resolution imaging of the same region in the L' band with NAOS+CONICA at the VLT (UT4). The study of the nebular scattered light points to an internal-illumination model for the eastern component (B2). This model is confirmed by the detection of a point-like source in the L' -band data. In the western component (B1) the observed NIR colours of star 82 are consistent with spectral types B1a or early O V, while star 83 is reproduced by a B0 V. Therefore, we identify these objects as the main detected ionising sources. However, in terms of illumination, our polarimetric map indicates that these two stars are not the dominating illuminators of the reflection nebula. Illumination from multiple sources (possibly still undetected) seems to influence the polarisation pattern for this component. Geometric considerations in the calculation of the energetics of this region, combined with the knowledge of the detected stellar content, also points to the presence of other ionising sources. Our study reinforces the hypothesis that there is a champagne flow towards the south-west part of the region.

Key words. techniques: polarimetric – techniques: high angular resolution – stars: formation – ISM: HII regions – ISM: reflection nebulae

1. Introduction

The question of how massive stars form remains an open problem. The determination of the basic units that will form massive stars within a molecular cloud, identification and isolation of the evolutionary stages and subsequent interaction with the surrounding material are currently under discussion (see Garay & Lizano 1999; Henning & Stecklum 2000).

The first step towards understanding massive star formation is the study of the cause and progress of the collapse phase. However, massive star formation in the early stages is difficult to access observationally. Massive stars have short lifetimes ($\sim 10^7$ years), are deeply embedded in molecular

cloud cores, and often are formed in clusters with complicated morphologies.

Massive star formation certainly begins with a phase in which the molecular cloud collapses into smaller fragments. Such fragments later develop into the so-called *Hot Cores*. These Hot Cores are characterised by high extinction ($A_V > 50$ mag) and can host more than one young stellar object (Churchwell 1998). When the stars are fully formed, the rate of Lyman continuum photons emitted is large enough to ionise the surrounding material. These ionised regions, small in diameter (~ 0.01 – 0.1 pc) and known as ultra-compact HII regions (Wood & Churchwell 1989, hereafter WC89), are among the earliest accessible stages after the formation of massive stars. Massive stars tend to form in a gregarious way (Ho & Haschick 1981; Welch et al. 1987; Rudolph et al. 1990). This results in complex morphologies for the HII regions (Garay et al. 1993). Non-spherical morphologies are detected for UCHII regions that do not harbour luminous massive stars. Instead, they are interpreted as externally ionised objects inside larger inhomogeneous HII regions (Hartquist & Dyson 1993).

* Visiting Astronomer, German-Spanish Astronomical Centre, Calar Alto, operated by the Max-Planck-Institute for Astronomy, Heidelberg, jointly with the Spanish National Commission for Astronomy.

** Based on observations collected at the European Southern Observatory, Paranal, Chile (ESO Programme 71.C-0143(A)).

To understand the star formation mechanism, it is extremely important to obtain observational constraints for some of the crucial parameters of these regions, e.g. spectral type and location of ionising stars, physical properties of the surrounding gas and molecular cloud, and overall stellar content. Morphological studies reveal the interaction of massive stars with the surrounding molecular cloud and the role of stellar winds and outflows, casting some light on the paradox of the apparent long lifetime of the UCH_{II}s (WC89).

Only recently has the observation of these objects in the NIR, sometimes complemented with AO techniques, achieved sufficient spatial resolution and sensitivity to resolve, at least partially, their stellar population, and to identify some of the ionising sources (Watson & Hanson 1997; Feldt et al. 1998; Henning et al. 2001; Okamoto et al. 2003; Feldt et al. 2003). Broad- and narrow-band NIR imaging provides an accurate determination of the morphology of the reflection nebula and the ionised material at subarcsecond resolution. The comparison of images obtained in the hydrogen recombination lines with radio-continuum maps can be used to constrain the extinction produced by the foreground material.

NIR polarimetry provides additional information, pinpointing stars hidden by dust in the molecular cloud. If the cloud is optically thin, single scattering will dominate, producing a centrosymmetric pattern of the polarisation vectors centred at the illuminating source (Weintraub & Kastner 1993; Weintraub et al. 1994; Henning & Stecklum 2002).

In this paper, high-resolution polarimetric and photometric observations are used to investigate in detail the UCH_{II} region G61.48+0.09. The relatively small distance (we adopt 2.5 kpc; Goetz et al. 1999; Deharveng et al. 2000), as well as the high quality of the existing radio continuum maps, combined with the high spatial resolution achieved in NIR imaging make this source an excellent object for pushing further the limits of current knowledge of the stellar content and the physical properties of the surrounding material in UCH_{II}s.

2. The G61.48+0.09 region

G61.48+0.09 is a complex of two UCH_{II} regions (G61.48+0.09A and G61.48+0.09B), located in the emission nebula Sh2-88B. They were first identified on the red print of the Palomar Sky Survey and studied in the radio continuum by Felli & Harten (1981). In the same paper, G61.48+0.09B was catalogued as a complex object with two ionised components B1 and B2, with B1 dominant in terms of radio flux (Fig. 1). The component B2 is located to the east and has been classified as a spherical or unresolved UCH_{II} region which subtends an angular size of $\sim 3''.5$ on the sky (i.e. 0.04 pc at 2.5 kpc), whereas B1 is an extended cometary region ($\sim 14''$, i.e. 0.17 pc) that is thought to undergo a champagne flow (Garay et al. 1994, 1998a,b). Note that WC89 denoted the B2 peak of Garay et al. (1993) as G61.48+0.09A. Figure 79 in WC89 does not show the peak associated with the B1 component. However, it is present in the full-size 6 cm image that we obtained from the on-line version of the paper. Figure 80 in WC89 shows another peak of compact emission

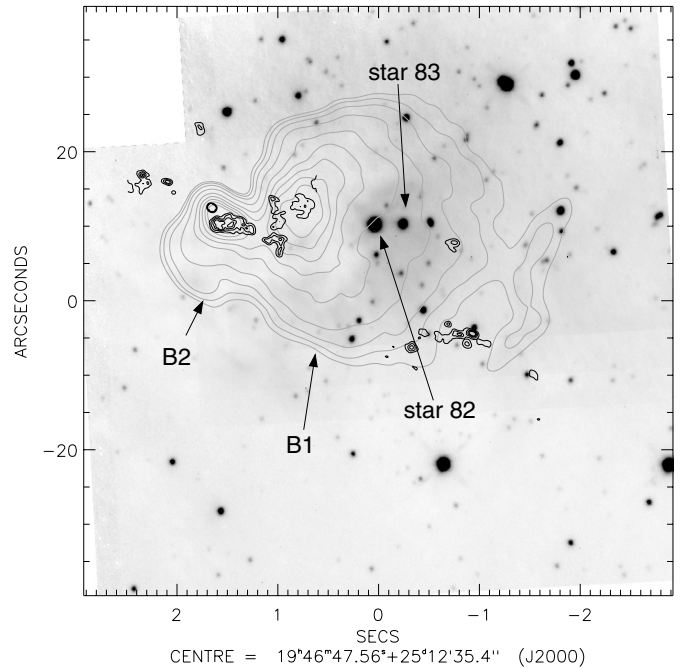


Fig. 1. K' -band image of G61.48+0.09B on a logarithmic scale (between 35 mJy/arcsec² and 40 mJy/arcsec²), obtained using the AO system ALFA (Alvarez et al. 2004, in preparation.). The grey contours correspond to the 6 cm continuum emission with a resolution of 3'' obtained with the VLA in C configuration (kindly provided by G. Garay). Contours are at flux values of 5, 8, 13, 25, 51, 76, 102, 127 and 152 mJy/beam. The lowest contour corresponds to a 20σ detection. The black contours indicate the 6 cm continuum emission with VLA in A configuration with a resolution of 0''.4 (WC89), highlighting the peaks in the emission. Contours are at 0.2, 1.6, 3.0, 4.4, 5.8 and 7.2 mJy/beam. The lowest contour corresponds to 1σ . Star 82 and star 83 follow the notation of Deharveng et al. (2000).

(G61.48+0.09B) which is located at the south-western edge of B1 (see Fig. 1).

The analysis of the velocity structure of CO lines in Sh2-88B showed the presence of molecular gas in the region and its association with the H_{II} region (Schwartz et al. 1973; Blair et al. 1975). The CO data reveal higher densities at the locations of the B1 and B2 components, explaining why no NIR counterparts are detected. The density decreases dramatically at the border of the detected H α nebulosity (Deharveng & Maucherat 1978). A molecular outflow was also identified (Phillips & Mampaso 1991) and confirmed later by White & Fridlund (1992). However, these last authors admit the possibility of more than one outflow within the molecular cloud, thus explaining its complexity and the presence of substructures.

The first NIR study of G61.48+0.09 was performed by Evans et al. (1981) with a resolution of 16''. Later, the 2.2 μ m emission peak was resolved into a *trapezium system* of three stars (Deharveng et al. 2000). However, only part of the region traced by the radio-continuum emission and associated to the component B1 is visible at NIR wavelengths. The ionising source of this UCH_{II} region was identified as star 82, the most eastern star within the trapezium, based on the high luminosity shown in the colour-magnitude diagram and its central location with respect to the radio-continuum

Table 1. Observational data.

Filter	IT^a (s)	$FWHM^b$ (")	Reference star	mag/band
K' + wire-grid	120×5	0.6	GSC02114300957	12.96/ V
Bry	150×5	0.5	GSC02114300957, GSC02114300691	12.88, 12.96/ V
H_2	150×5	0.5	GSC02114300957, GSC02114300691	12.88, 12.96/ V
L'	29	0.13	Star 82	9.4/ K_s

^a Integration time.

^b Spatial resolution at the reference star.

emission. Deharveng et al. (2000) assigned a spectral type between O8.5V and O9.5V to this star. However, Evans et al. (1981) and Garay et al. (1998a,b) explained the cometary morphology as produced by a champagne flow, the head of which is further east than star 82, near the 6 cm continuum peak.

G61.48+0.09 is associated with a very extended NIR nebula ($\sim 30''$; Deharveng et al. 2000) to the south-west, which was partially traced in $H\alpha$ emission (Deharveng & Maucherat 1978). The $H\alpha$ emission from diffuse gas is detected at a relative velocity of $\sim 3 \text{ km s}^{-1}$ with respect to the molecular cloud, which favours the presence of a flow. Evans et al. (1981) suggested that the gas traces a cavity in the front face of the molecular cloud.

Some immediate questions arise regarding this complex source. Can we pinpoint sources still embedded in the dense molecular cloud at NIR wavelengths through the scattered light traced by a linear polarisation map in the K' band? Once we know the spatial distribution of the extinction, can we constrain better the photometric information on those stars that are detected in the NIR in order to identify the star or stars that are producing the $H\text{II}$ region? Is there any emission produced by shocked molecular hydrogen that confirms the existence of an outflow and its direction?

3. Observations and data reduction

The UCHII region G61.48+0.09 was observed during the nights of November 11 and 12, 2000, using the Adaptive Optics system ALFA (Kasper et al. 2000) with the NIR camera Omega-Cass (Lenzen et al. 1998a) at the 3.5 m telescope on Calar Alto (Almeria, Spain). The reference star used by the AO system for the polarimetric images is located at $\alpha_{2000} = 19^{\text{h}}46^{\text{m}}47^{\text{s}}$, $\delta_{2000} = +25^{\circ}12'13''$ (see Table 1). For the narrow-band images we used two reference stars ($\alpha_{2000} = 19^{\text{h}}46^{\text{m}}47^{\text{s}}$, $\delta_{2000} = +25^{\circ}12'13''$, $\alpha_{2000} = 19^{\text{h}}46^{\text{m}}46^{\text{s}}$, $\delta_{2000} = +25^{\circ}13'04''$), averaging after the two image sets. The pixelscale is $0''.08/\text{pixel}$. Polarimetric images were obtained with the K' -band filter ($\lambda = 2.118 \mu\text{m}$, $\Delta\lambda = 0.35 \mu\text{m}$), whereas imaging of the Bry and $H_2(1-0)S1$ emission was performed with the NB2.166 ($\Delta\lambda = 23.2 \text{ nm}$) and the NB2.122 ($\Delta\lambda = 22.8 \text{ nm}$) filters, respectively.

AO-assisted L' -band images ($\lambda = 3.8 \mu\text{m}$, $\Delta\lambda = 0.62 \mu\text{m}$) were obtained on June 12th, 2003 at the VLT/UT4 with the L27 camera of NAOS/CONICA (Rousset et al. 2000; Lenzen et al. 1998b). For these observations, star 82 served as the

reference of the NIR-wavefront sensor, using the N80C20-dichroic. The total exposure times and spatial resolutions achieved are summarised in Table 1.

3.1. Polarimetric observations: K'

Besides the NIR imaging and spectroscopy modes, a polarimetric facility is available for ALFA/Omega-Cass. The polariser consists of four wire-grids oriented in four different directions (0° , 45° , 90° and 135°) with transmission efficiencies of 87%, 97% and 90%, relative to the 45° wire-grid.

For every polariser, 5 exposures of 120 s integration time were obtained with slight offsets between them, in order to construct a sky image for each single orientation. For flat-fielding, sky subtraction and bad-pixel flagging, via the *variation method* (Ageorges & Walsh 1999) with dome flats, the standard IR reduction techniques were followed. After registration of the four images with IRAF¹, spatial binning with a 4×4 box was necessary to increase the signal-to-noise ratio (SNR). We derived the Stokes parameters from the differences between the intensities of the four orientations, and determined the polarisation degree and angle of the polarisation vectors (Serkowski 1962). Debiasing of the polarisation degree through the Wardle and Kronberg estimator accounts for the fact that the noise produces a bias in the estimate of the polarisation degree (p) (Serkowski 1958; Simmons & Stewart 1985). The error in the polarisation degree (σ_p) was determined by the Gaussian propagation of the sky error (dominant in the NIR images with long exposure times) for signal-to-noise values higher than 6. For smaller SNRs, the 1σ -confidence interval calculation (Simmons & Stewart 1985) was applied. The error in the position angle was calculated using the expression $\sigma_\theta = 28.648(\sigma_p/p)$ when $p/\sigma_p > 6$ (Serkowski 1962). The expression from the error distribution of σ_θ that appears in Naghizadeh-Khouei & Clarke (1993) was used for $p/\sigma_p < 6$.

Calibration of the instrumental polarisation is performed by using the intensities of 17 field stars within the images and assuming them to be – at least on average – unpolarised. Observations of the polarised standard star HD 38563C, from the Whittet et al. (1992) catalogue, were used to correct the

¹ IRAF is distributed by the National Optical Astronomy Observatories, which is operated by the Association of Universities for Research in Astronomy, Inc. (AURA) under cooperative agreement with the National Science Foundation.

zero point of the polarisation angle and the average polarisation efficiency.

3.2. Narrow-band imaging: B_{ry} and H_2

In an analogous way, narrow-band images of the B_{ry} and H_2 emission were obtained in 5 offset positions with integration times of 150 s in every filter, for two sets of images. We used a different reference star for each of them (Table 1). No narrow-band images of the adjacent continuum were taken for calibration. We scaled the flux in the K' -band image to the width of the narrow-band filters, assuming that the bulk of the emission is continuum. The scaled continuum image was subtracted from the H_2 image, showing the absence of line emission. Therefore we used the H_2 image as continuum for subtraction from the B_{ry} image. Since no photometric standard was observed, J -, H - and K' -calibrated-aperture photometry on 5 stars in the field was used to interpolate and calibrate the flux density of the final B_{ry} and H_2 images.

3.3. Broad-band imaging: L'

L' -band images with NAOS/CONICA at the VLT were obtained with the chopping-nodding technique in order to correct for the thermal background noise. However, technical problems only allowed chopping with a throw of $20''$ and a total integration time of 29 s. This results in a sub-optimal subtraction of the background, limiting our study to point-like sources, and does not allow us to investigate any extended emission in the L' -wavelength range. Flux calibration was performed by observing the standard star HD 106965 with the same optical set-up, but jittering over the field in order to construct a median-sky.

4. Results and discussion

4.1. The illuminating source

Figure 3 shows our complex polarimetric map of G61.48+0.09 in the K' band. Polarised light is present across the entire extension of the nebula; but we only depict vectors with polarisation degrees between 10% and 80% to exclude depolarisation produced by multiple scattering and noise in very faint regions, respectively. The polarisation degree grows toward the edges of the nebula, attaining values of up to 35%. In such cases, the polarisation induced by the interstellar medium is negligible ($\sim 2\%$, cf. Ageorges & Walsh 1999). The presence of several stars in the region of nebular emission limits the area where we can extract information about the illuminating sources. To determine the location of the illuminating source, we apply the method proposed by Weintraub et al. (1993), which calculates the intersection of the perpendicular to every pair of vectors, over arbitrarily selected areas. These areas must show an increasing polarisation degree with the distance to the presumed illuminating source. The average of these positions, using the signal-to-noise ratio of the polarisation angle as weighting factor, produces an estimate for the source position, including a

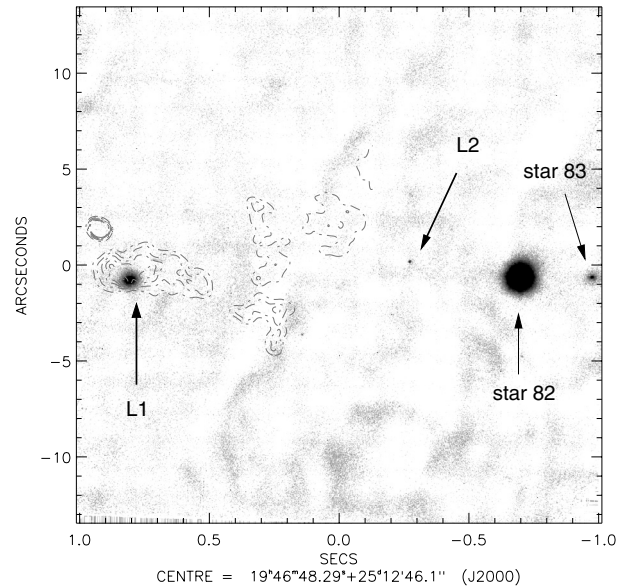


Fig. 2. L' -band image with NACO at the VLT. The grey-scale varies from $0.07 \text{ Jy}/\square''$ (white) to $0.2 \text{ Jy}/\square''$ (dark). Two stars not detected in the J , H and K' band are now located above the 3σ threshold (L1 and L2). The grey-dashed contours correspond to the 6 cm VLA map (Wood & Churchwell 1989).

certain error. We focus our analysis of this polarisation map on different areas around the two UCHII regions.

- (1) The two knots of emission (knot 1 and knot 2 in Fig. 3a), located at $\alpha_{2000} = 19^{\text{h}}46^{\text{m}}49^{\text{s}}.3$, $\delta_{2000} = +25^{\circ}12'36''$ and $\alpha_{2000} = 19^{\text{h}}46^{\text{m}}49^{\text{s}}.0$, $\delta_{2000} = +25^{\circ}12'26''$ respectively, exhibit a partially centrosymmetric pattern. This pattern is compatible with the centre being at the location of the B2 component. Both regions show a high degree of polarisation and a good signal-to-noise ratio. Figure 3a shows the positional error ellipse within a 99% certainty limit, using only the vectors in knot 1. In Fig. 3b, we consider also the vectors in knot 2. In both cases, the location of the illuminating source is consistent with the position of the B2 component traced by the 6 cm map. Thus, we conclude that the B2 component is internally illuminated. Figure 2 shows the L' -band image in which two new sources (L1 and L2), not present in the J -, H - and K' -band images, are detected with brightnesses of $m_{L'} = 8.0 \pm 0.1 \text{ mag}$ and $m_{L'} = 11.5 \pm 0.1 \text{ mag}$, respectively. As seen in the figure, the position of source L1 coincides with the peak of the radio map at the location of B2, confirming our polarimetric results.
- (2) The polarisation map around the location of the B1 component is very complex, i.e. there are many possible illuminating sources. In addition, the extinction produced by the molecular cloud is very high, leading to strong depolarisation. Most of the polarisation is concentrated at the edges of the molecular cloud (see Deharveng et al. 2000, for a comparison with the CO emission). Due to the absence of a global centrosymmetric pattern, we focus on the local analysis of the map and the comparison with the different hypotheses related to the possible stellar population.

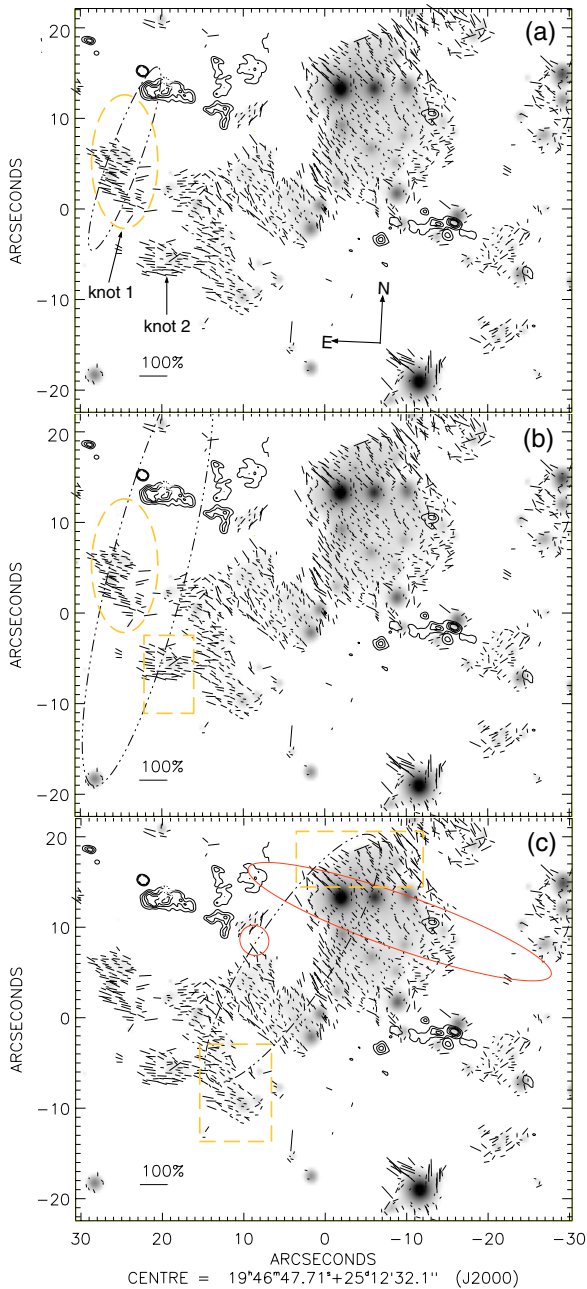


Fig. 3. K' -band polarisation map of G61.48+0.09. Each of the three panels represents a different estimate of the position of the illuminating source. The black dot-dashed ellipses indicate the region where the illuminating source is located; calculated through Weintraub’s method using the polarisation vectors located within the grey-dashed lines. The greyscale indicates the total polarised intensity, masked out according to our constraints of polarisation degree between 10 and 80%. Only one of every four vectors has been represented for clarity. The 100% polarisation vector is represented in the lower left corner of each panel. The grey-solid circle in panel c) indicates the 1σ -error of the MSX point source position. The grey-solid 1σ -error ellipse represents the IRAS source position. The black contours represent the 6 cm continuum emission from the VLA in A configuration.

The first possibility is that the most luminous star at NIR wavelengths (star 82) is the main illuminating source, which was also proposed by Deharveng et al. (2000) to

ionise the region. However, the northern rim of the nebula, close to this star and where the signal-to-noise ratio is higher, shows no evidence of a dominant illumination coming from star 82. The second possibility is that, as we showed in the case of the B2 component, other undetected stars remain hidden to the observer at shorter wavelengths but still illuminate the nebula. No star is detected in the NIR images at the position of the B1 radio continuum peak, due to the high extinction. An MSX source is located $\sim 3''$ to the south-west of the radio peak, coinciding with the tail of the arc. Note that even though the resolution of the MSX catalogue is low, the accuracy in the source position is high ($\sim 2''$). Hence, it is likely that hidden stellar sources may be located near the MSX source or near the peak shown by the radio maps, just like in the case of G29.96-0.02 (Pratap et al. 1999). To test this, areas with vectors perpendicular to the radio peak were selected (squared areas in Fig. 3c). The resulting position ellipse is displaced from this source, but also close to the position of the MSX source, and includes the location of L2. Altogether, we find no evidence of star 82 being the main illuminating source of the nebula but most likely other embedded objects, such as L2, might contribute significantly to the illumination.

4.2. B_{ry} emission and extinction

Our B_{ry} map is shown in Fig. 4. The estimate of the B_{ry} -line emission within a circular aperture of $17''$ diameter, centered at $\alpha_{2000} = 19^{\text{h}}46^{\text{m}}47^{\text{s}}.1$ and $\delta_{2000} = +25^{\circ}12'43''$, yields a flux density of 0.15 ± 0.08 Jy. The quoted error results from the propagation of the error in the flux calibration and the error in the aperture photometry. This flux density is consistent with the 0.16 ± 0.02 Jy estimated by Goetz et al. (1999), within the same aperture, with poorer spatial resolution.

The B_{ry} emission around the B2 component is very faint and coincides with knot 1 (see Fig. 4). The bulk of the B_{ry} emission traces the south-west quadrant of the radio continuum map for component B1, at the same location as the reflection nebula. $H\alpha$ emission is also present in the same direction (Deharveng et al. 2000). Both features are consistent with the low density inferred from the CO map of this region (White & Fridlund 1992).

Star 82 is the only stellar source clearly visible as a point source in the continuum-subtracted B_{ry} image (see Fig. 4). This feature is also detected in a K -band spectrum, not shown in this paper. The rest of the stars in the field are well cancelled by the subtraction of the continuum. The $FWHM$ of the point-like source ($0''.5$) is of the same order as in the unsubtracted image (i.e. unresolved), and hence originates within a region of ~ 1200 AU around the star. The B_{ry} flux density integrated over an aperture of radius $1''$, centered at the position of star 82 was 15 ± 8 mJy (i.e. 0.01 mag in K_s , after the colour-correction derived from Alvarez et al. 2004).

The extinction map toward G61.48+0.09 (Fig. 5) was obtained by comparing the expected B_{ry} flux, derived from the 6 cm radio map obtained by G. Garay with our B_{ry} image, once the remaining emission at star 82 was subtracted with the

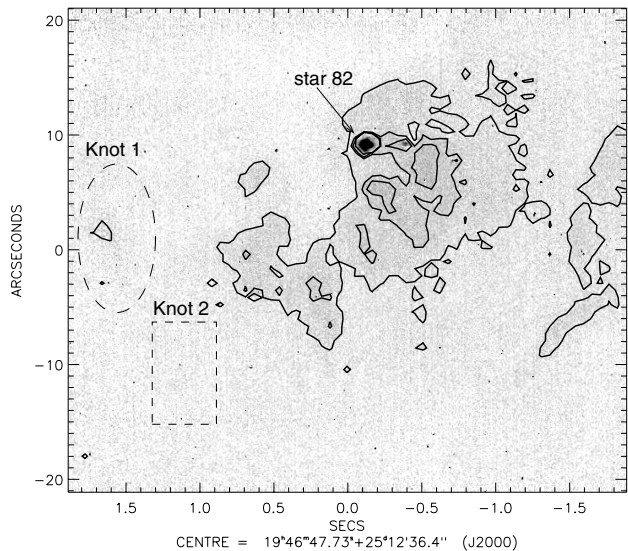


Fig. 4. Continuum-subtracted Bry image. Note the point-like remnant with a $FWHM$ of $0''.5$ at the position of star 82. Overlaid contours at 0.3, 0.6, 0.8 and $1.1 \text{ mJy}/\text{arcsec}^2$.

IRAF package DAOPHOT. The visual extinction map was obtained after convolving our Bry data to the resolution of the radio image ($\sim 3''$) in the same way as explained in Feldt et al. (1998), using the relation $A_V = 9.29A_K$ (Mathis 1990). The dominant error source is the calibration of the Bry flux, and the estimated error is approximately 2 visual magnitudes.

The map obtained with the same procedure as that used by Goetz et al. (2003) gives visual extinctions between 0 and 30 mag, in good agreement with theirs. Our estimate of the foreground extinction agrees also with the values derived from the photometry of selected stars (Goetz et al. 1999; Deharveng et al. 2000; Alvarez et al. 2004). This method estimates the extinction towards the ionised gas, and it must therefore be used as an approximation when correcting the stellar fluxes.

4.3. The ionising sources

4.3.1. The radio data

Radio continuum observations give an estimate of the spectral type of the dominant ionising star that can be combined with the near IR photometric information to better pinpoint the characteristics of the stellar content of UCH_{II}s.

A number of assumptions need to be made to derive the minimum rate of Lyman continuum photons needed to produce the free-free radiation, probed by the radio continuum data: a) the radio continuum emission is optically thin; b) the ionising source is unique and emits isotropically; c) all the diffuse radiation-field photons are absorbed very close to where they were generated (i.e. the *on-the-spot* approximation or case B recombination), not having any effect on the local ionisation state; d) an ionic abundance of only hydrogen. Under these assumptions, the minimum rate of Lyman continuum photons is estimated with Eqs. (1) and (3) of Kurtz et al. (1994). The calculation of the Lyman continuum photons, taking into account

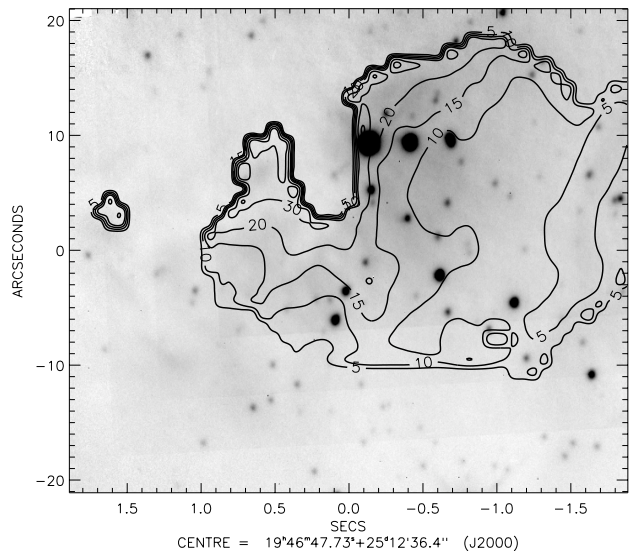


Fig. 5. Visual extinction map of G61.48+0.09 comparing the calculated Bry flux from the 6 cm continuum emission provided by G. Garay with our high-resolution Bry map convolved to the same resolution. The contours are labeled with the extinction values in magnitudes.

the ionic abundances He^+/H^+ by Simpson & Rubin (1990), leads to similar values.

Integrated flux densities for B1 and B2 at 6 cm were derived by Garay et al. (1993), leading to values of 4.36 Jy and 0.83 Jy respectively. They yield the rates of Lyman continuum photons $\log(N_{\text{Lyc}}) = 48.4$ for B1, and $\log(N_{\text{Lyc}}) = 47.7$ for B2. To calculate $\log(N_{\text{Lyc}})$ a distance of 2.5 kpc, an electron temperature of 10^4 K, an $u_1 = 0.775$ and $a \sim 1$ (Mezger & Henderson 1966) were used. Comparison of this emission with models of stellar atmospheres yields the spectral type of the ionising star, assuming that the main contribution to the ionisation comes from only one star. According to the models of Vacca et al. (1996), we infer spectral types of O9.5V and B1V or B2V² for components B1 and B2, respectively.

In the case of G61.48+0.09B1, where the morphology of the radio map is clearly cometary, there is a possible identification of a central ionising star, given by the NIR data. Observations of the kinematics of the H₉₂ α line show that this component of G61.48+0.09 is undergoing a champagne flow (Garay et al. 1994). According to model calculations by Yorke et al. (1983), the H_{II} region experiencing a champagne flow has an ionisation-bounded side towards the molecular cloud and a density-bounded side in the direction away from the cloud. These correspond to the *head* (peak) and the *tail* of the radio map for B1, respectively (see Fig. 1). For this reason, the case B approximation is not fully realistic for these sources, since part of the photons are *escaping* in the directions towards the tail.

The lower limit of the Lyman continuum photon rate is then inferred from the radio emission measured only in a sector of the map in the direction that connects the central star with the

² For the determination of these spectral types, we have used an extrapolation of the models of Vacca et al. (1996) to spectral types later than B0.5V.

maximum of the radio emission. The minimum angle of this sector is given by the resolution element (i.e. the beamsize) at the location of the peak emission. The obtained Lyman continuum photon rate must be divided by the solid angle, as seen by the star, that subtends this projected emission, and rescaled to all directions in order to obtain the total rate of Lyman continuum photons in the HII region. In the plane of the sky, the angular dimension of this solid angle is equal to the angle of the sector. The angular dimension of the solid angle in the line of sight must be assumed. We propose three possibilities: a) equal to the dimension in the plane of the sky; b) equivalent to the angle subtended by the $FWHM$ of the radio-peak continuum emission; c) all possible angles (i.e. 180°). Thus, the rescaling factors are $\frac{4\pi}{\Phi_B^2}$, $\frac{4\pi}{\Phi_B \cdot \Phi_{FWHM}}$ and $\frac{2\pi}{\Phi_B}$, respectively. The beamsize ($3''.05$) subtends an angle $\Phi_B = 20^\circ$ from the central star ($\alpha_{2000} = 19^h46^m47^s.6$, $\delta_{2000} = +25^\circ12'45''.6$), while the $FWHM$ subtends an angle of $\Phi_{FWHM} = 80^\circ$.

The rate of Lyman continuum photons inferred from the initial circular sector is $N_\Phi = 3 \times 10^{47}$ phot s^{-1} . After rescaling it for each of the three geometrical assumptions, the $\log(N_{Lyc})$ results into 49.5, 48.9 and 48.7 for cases a), b) and c), respectively. Hence, the corresponding spectral types of the central star, inferred from the stellar models, are those of a O.5, O8 and O8.5V star, respectively. Since we do not have further information of the structure in the direction of the line of sight, we will consider this range of spectral types (varying over 3.5 spectral subclasses) as the best approximation to the spectral type of the ionising central star of G61.48+0.09B1.

4.3.2. Can the NIR stellar content explain the energy budget?

Since L1 and L2 have only been detected at $3.5 \mu m$ (detection limits in J , H and K' band are 18.6, 18.2 and 16.5 mag, respectively), and there is no information at their location in the extinction map, no determination of the spectral types of these sources was attempted. The NIR colours of stars 82 and 83, and their central or close to central position within B1, indicate that these are two possible stellar candidates for ionising the HII region.

The spectral classification of star 82 is revised (Deharveng et al. 2000), based on our new determination of the extinction, new high resolution ($0''.57$) photometry in the J , H and K_s band (Alvarez et al. 2004) and our own photometry in the L' band.

The apparent magnitudes, $m_J = 16.1 \pm 0.1$ mag, $m_H = 12.2 \pm 0.1$ mag, $m_{K_s} = 9.4 \pm 0.2$ mag were calculated with DAOPHOT in IRAF, using the 2MASS³ Point Source Catalogue for flux calibration (Alvarez et al. 2004). We have subtracted from the K_s magnitude 0.01 mag associated with the residual Br γ emission (see Sect. 4.2). In the L' band, a $m_{L'} = 5.4 \pm 0.1$ mag was determined with aperture photometry,

³ This publication makes use of data products from the Two Micron All Sky Survey, which is a joint project of the University of Massachusetts and the Infrared Processing and Analysis Center/California Institute of Technology, funded by the National Aeronautics and Space Administration and the National Science Foundation.

and the error was estimated by taking into account the uncertainty in the flux calibration. Due to the Br γ emission of star 82, the value of the extinction ($A_V = 24 \pm 2$ mag, see Fig. 5) must be considered as an approximation at this location. Moreover, the PSF subtraction, described in Sect. 4.2, provides a lower limit to this value, since it only accounts for foreground extinction and not for intrinsic extinction.

In Fig. 7, we show the spectral energy distribution (SED) of star 82 in the J , H , K_s and L' bands. The observed SED is compared with theoretical SEDs of early type dwarfs (luminosity class V) and supergiants (luminosity class Ia). We take the absolute magnitudes (M_V) from Vacca et al. (1996) with spectral types in the range O3–B0 for dwarfs, and in the range O3–O9 for supergiants. For later spectral types, we use values from Drilling & Landolt (2000). The intrinsic colours have been chosen from Wegner (1994), because they describe spectral types up to O6/O5. Since the observed J magnitude is less likely to be affected by an intrinsic excess, we utilise the J magnitude and the $J - H$ colour as fitting criteria. Besides, we discard an excess in the J magnitude due to scattering because the J image of Deharveng et al. (2000) shows that absorption clearly dominates at the position of star 82. The latest dwarf spectral type that reproduces the observed J -band flux of star 82, considering $A_V = 24 \pm 2$ mag (see Fig. 5), is a B1V (see Fig. 7a). Earlier types with higher extinction values fit better the SED of star 82. However, even an O3V star (the earliest available) is well below the observed fluxes at H , K_s and L' bands. This might be caused by the presence of an excess in the local extinction (e.g. a disc). Another possibility is that the grain composition near the star is different from that in the interstellar medium.

Supergiants show stronger fluxes for the same spectral types as dwarfs. In contrast to what is observed for dwarfs, supergiants grow in luminosity at NIR wavelengths with later spectral types. Therefore, in the case of star 82, an increase of the extinction favours the B-types. The J magnitude and the $J - H$ colour is better reproduced by a late B star with $A_V = 37$ mag, but the range of possible spectral types spreads from O9I ($A_V = 36$ mag) to A0I ($A_V = 37$ mag). Yet the emission of star 82 in the K_s -band starts to be higher than predicted by the stellar models and shows a clear excess at $3.5 \mu m$.

The use of the $J-H-K$ photometry from Deharveng et al. (2000) yields similar results for both luminosity classes. Continuum excesses in the range of $2-10 \mu m$ are known to be present in B[e]-supergiants due to circumstellar dust (Zickgraf et al. 1986). The hypothesis that this star is a supergiant is consistent with the Br γ emission detected toward star 82, predicted by the models of spectral evolution of massive stars (Schaerer et al. 1996), which appears to be statistically more frequent among supergiants (Hanson et al. 1996). Therefore, our data of star 82 is best reproduced by the spectral type of a B or late O supergiant.

Figures 7c and 7d show the SED of star 83, compared with the theoretical SEDs of early-type dwarfs and supergiants. We used $m_J = 13.4 \pm 0.1$ mag, $m_H = 11.8 \pm 0.1$ mag, $m_{K_s} = 10.8 \pm 0.1$ mag and $m_{L'} = 9.3 \pm 0.1$ mag, which were calculated in the same way as previously described for star 82. The theoretical SEDs were extinguished by an $A_V = 15 \pm 2$ mag, derived from our extinction map. From Fig. 7d, we discard the

possibility that star 83 is a supergiant because they are too luminous to reproduce the observed SED. Models of dwarfs under a visual extinction of 15 mag appear to be more suitable to describe star 83. Since star 83 is located well within the reflection nebosity (see Fig. 2 in Deharveng et al. 2000), we expect that there is some contribution of scattered light to the J magnitude. Therefore, we use the H magnitude and the $H - K_s$ colour as fitting criteria. Figure 7c illustrates that a B0V spectral type can approximately explain the observed colours of star 83.

These estimates of spectral types must be considered with caution, since they are strongly affected by numerous uncertainties: the distance to the object, the method to determine the extinction, the presence of scattered light, etc.

If we take into account the two possible luminosity classes for star 82 estimated above, the combination of the spectral type of star 82 and star 83 amounts a logarithm of the rate of ionising photons in the range 47.0–49.9⁴, if star 82 is a dwarf star, and <49.4 if star 82 is a supergiant. The estimate provided by the radio map, discussed in the former section, lies between $\log(N_{\text{Lyc}}) = 48.7\text{--}49.5$. These ranges are represented in Fig. 6. The estimate that considers star 82 to be a dwarf includes values above the overlapping region, meaning that this star would be enough to produce the entire rate of Lyman continuum photons, derived from the radio continuum map. These early spectral types of dwarfs fit best the SED of star 82. Both models of dwarfs and supergiants show values below the overlapping region. Should the true spectral type of star 82 be contained in one of these best-fit regions, additional ionizing sources would be needed to explain the Lyman continuum photon rate. The best fit in the supergiant model corresponds to this regime. The polarimetric map and the presence of an excess of $\text{Br}\gamma$ support this last hypothesis, indicating that L2 or possible undetected sources are contributing to the ionisation. However, NIR spectroscopy is mandatory to discriminate between these two possible spectral types for star 82 (dwarf/supergiant). If the classification of star 82 as a supergiant is confirmed by further observations, then an age spread might be responsible for the increasing size of the HII regions to the west (B1 component is a compact region), instead of the density gradient of the surrounding material. The use of more recent stellar models of Schaerer et al. (1997) and Smith et al. (2002) leads to a similar conclusion.

4.3.3. Morphology

Figure 8 shows the structure of the $\text{Br}\gamma$ -line map, the radio-continuum emission and the scattered light in the nebula. The ionised material, traced by the $\text{Br}\gamma$ contours, is coincident with part of the continuum nebular emission. This common area appears dimmer in the 6 cm map, where the flux density drops faster. The polarised intensity over this area is very small and even negligible in many points. Considering the small extinction, an absence of scatterers can explain this effect.

The lack of $\text{Br}\gamma$ emission over the rest of the B1 UCHII region (toward the north-east) is, very likely, due to the

⁴ The contribution of star 83 is considered constant and lower than $\log(N_{\text{Lyc}}) = 48.2$.

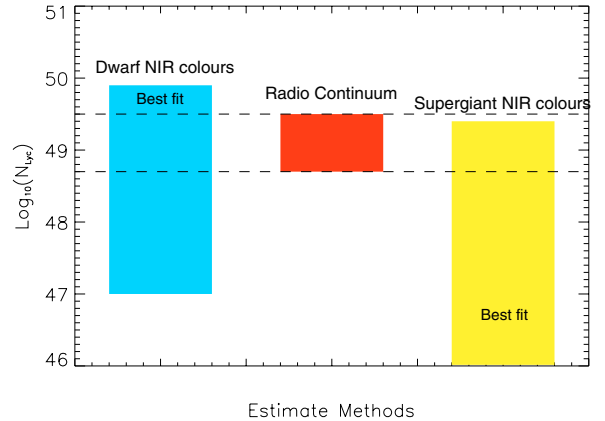


Fig. 6. Comparison of the Lyman continuum photon rates, estimated through the radio-continuum map, and those modelled by the NIR colours of star 82, considering luminosity classes of dwarfs and supergiants.

foreground extinction caused by the molecular cloud. The northern rim of the nebula, and, in general, the edges of the molecular cloud show a stronger scattered signal. In general, the $\text{Br}\gamma$ line emission is very faint, but in these regions the extinction rises and the line is no longer detected. Instead, the polarised intensity grows. These regions would correspond to the walls of a cavity opened by a champagne flow, evolving toward the south-west, since no scattering particles are present in the direction toward lower densities of the molecular cloud.

4.4. Shocked molecular hydrogen – the outflow

It was expected that the presence of a molecular outflow (Philips & Mampaso 1991; White & Friedlund 1992) would be traced in the $\text{H}_2(1-0) \text{ S}(1)$ line. Narrow-band images at $2.12 \mu\text{m}$, after subtraction of the continuum, do not show H_2 emission. Our detection limit in this image is $3.5 \times 10^{-4} \text{ Jy}/\square''$. Therefore, the upper limit for the extinction-corrected line intensity produced in areas where $A_V \sim 10 \text{ mag}$ (i.e. $\sim 0.25 \text{ pc}$ from star 82) is $8.9 \times 10^{-4} \text{ Jy}/\square''$, and where $A_V \sim 20 \text{ mag}$ (i.e. 0.02 pc from star 82) is $2.4 \times 10^{-3} \text{ Jy}/\square''$. These detection thresholds are compared with models of magnetohydrodynamic shock waves propagating at speeds between 5 and 50 km s^{-1} in molecular clouds (Draine et al. 1983). The kinematics of the molecular cloud (Schwartz et al. 1973; Blair et al. 1975) results in an average outflow velocity of $\sim 20 \text{ km s}^{-1}$. Assuming that the outflow collides with the static surroundings, the models predict intensities lower than $1.6 \times 10^{-5} \text{ Jy}/\square''$ (for densities around 10^4 cm^{-3} and B_0 between 50 and $100 \mu\text{G}$) and higher than $1.6 \times 10^{-3} \text{ Jy}/\square''$ (for densities higher than 10^6 cm^{-3} and B_0 between 500 and $1000 \mu\text{G}$). Hence, our detection limit can exclude the presence of a shock at speeds $>20 \text{ km s}^{-1}$ for the second case. However, our data cannot exclude the presence of shocks in the first scenario.

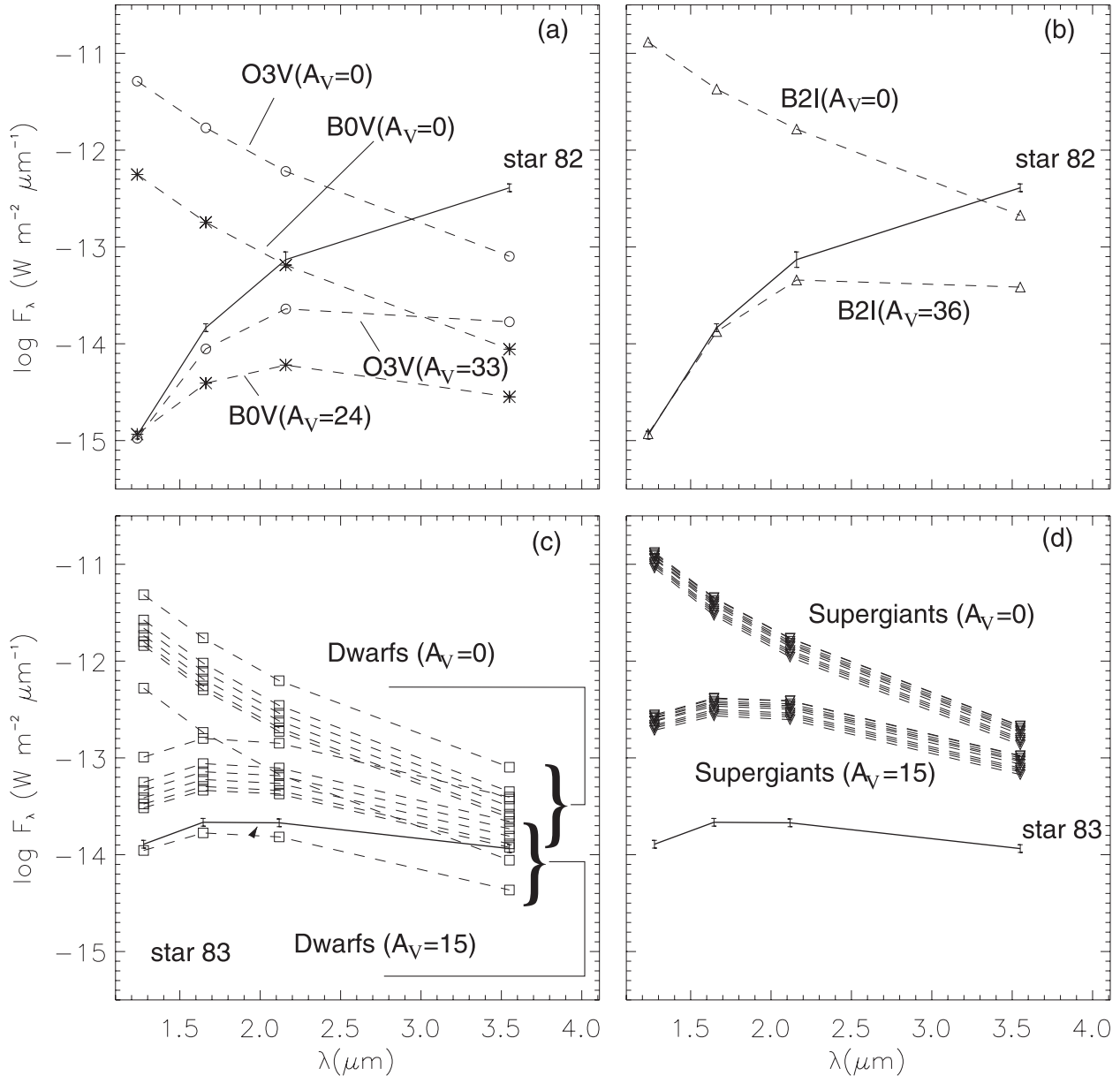


Fig. 7. Comparison of the spectral energy distributions of star 82 and star 83 with stellar models at different visual extinctions. A distance of 2.5 kpc has been assumed. **a)** Comparison of star 82 with stars of luminosity class V. **b)** Comparison of star 82 with stars of luminosity class I. **c)** Comparison of star 83 with stars of luminosity class V in the range O3–B1. **d)** Comparison of star 83 with stars of luminosity class I in the range O3–B1.

5. Conclusions

We have presented a high-resolution study of the UCH_{II} region G61.48+0.09 at NIR wavelengths. We have resolved individual stellar components and studied the extended nebulosity associated with the H_{II} region. Our K' -band polarimetric map indicates that the B2 component is internally illuminated and we confirm the presence of a point-like source at the same location in our L' -band image obtained with NACO. The polarisation data also show that star 82 cannot be the main illuminating source of the nebula, and that the contribution of other (undetected) stars is important.

A high resolution extinction map is used in combination with new NIR photometry, and the Bry emission for star 82,

to constrain the spectral type of the main ionising detected stars (star 82, star 83). The NIR SED of star 82 is compatible with a O3V–B1V star, with NIR excess in H , K_s and L' or with a supergiant in the range O9Ia–A0Ia, showing an IR excess at $3.5 \mu\text{m}$. The spectral type of star 83 is compatible with a B0V star. The combined energy budget of these two stars (if star 82 is an O9Ia star) appears to be sufficient to produce the rate of Lyman continuum photons in the B1 component inferred from the 6 cm map. This calculation assumes that the entire radio-emitting region is ionisation-bounded. However, since B1 is cometary (and therefore not ionisation-bounded) if we consider only the Lyman-continuum-photon rate necessary to ionise the radio peak of the B1 component and rescale it to the rest of the region, assuming a central isotropic

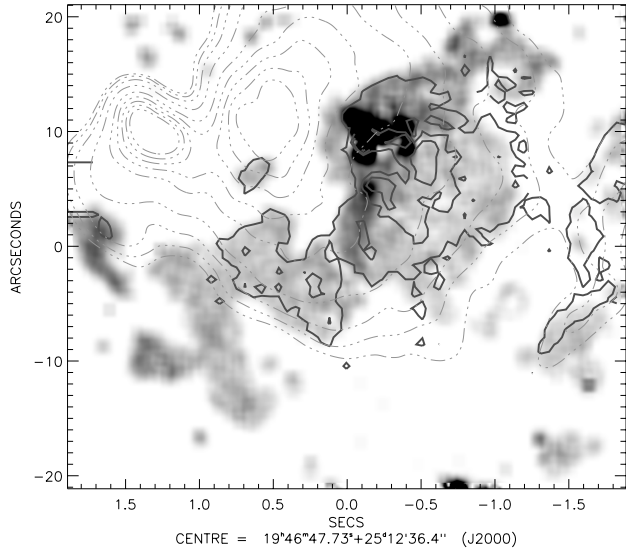


Fig. 8. Image of the polarised intensity in G61.48+0.09. The solid lines represent the Bry line emission with contours at 0.3, 0.6, 0.8 and 1.1 mJy/arcsecond squared. The dotted line corresponds to the 6 cm map with contours at 5, 8, 13, 25, 51, 76, 102, 127 and 152 mJy/beam.

radiating source, some of the spectral types that reproduce the NIR colours of star 82 and star 83 cannot justify this rate. This would mean that star 82 and star 83 are not the only ionising sources. Since a new star is detected close to the radio-continuum peak with an exposure time of only 29 s in the L' band, we expect to find more embedded sources in future deep L' - and M' -band images.

An upper limit for the $H_2(1-0) S(1)$ emission is found, which cannot exclude the presence of shocks in lower-density scenarios with B_0 between 50 and 100 μG , but does exclude the existence of shocks if the density is higher than 10^5 cm^{-3} and B_0 between 500 and 1000 μG .

The combination of the Bry and polarisation maps reveals that ionised gas dominates the emission in the south-west region of the nebulosity, suggesting a lack of scattering particles. Toward the north-east scattering gradually begins to dominate and finally drops where the extinction rises sharply. This indicates that we are looking at the foreground wall of the cavity in extinction (north-east) and to the background wall from the scattered light (south west). This picture reinforces the champagne flow model proposed by Garay et al. (1993).

Acknowledgements. This research has made use of the NASA/IPAC Infrared Science Archive, which is operated by the Jet Propulsion Laboratory, California Institute of Technology, under contract with the National Aeronautics and Space Administration.

We would like to thank J. Aceituno for his useful assistance during the observations at Calar Alto. E. Puga would like to thank G. Garay, who provided us with the 6 cm radio map in D configuration, and D. Butler for the careful reading of this manuscript.

References

Alvarez, C., et al. 2004, ApJS, accepted
 Ageorges, N., & Walsh, J. R. 1999, A&AS, 138, 163
 Blair, G. N., Peters, W. L., & vanden Bout, P. A. 1975, ApJ, 200, L161

Deharveng, L., Nadeau, D., Zavagno, A., et al. 2000, A&A, 360, 1107
 Deharveng, L., & Maucherat, M. 1978, A&A, 70, 19
 Draine, B. T., Roberge, W. G., & Dalgarno, A. 1983, ApJ, 264, 485
 Evans, N. J., Harvey, P., Israel, F., et al. 1981, ApJ, 250, 200
 Feldt, M., Stecklum, B., Henning, Th., et al. 1998, A&A, 339, 759
 Feldt, M., Puga, E., Lenzen, R., et al. 2003, ApJ, 599, L91
 Felli, M., & Harten, R. H. 1981, A&A, 100, 42
 Garay, G., & Lizano, S. 1999, PASP, 111, 1049
 Garay, G., Gomez, Y., Lizano, S., et al. 1998a, ApJ, 501, 699
 Garay, G., Gomez, Y., Lizano, S., et al. 1998b, ApJ, 501, 710
 Garay, G., Lizano, S., & Gomez, Y. 1994, ApJ, 429, 268
 Garay, G., Rodriguez, L. F., Moran, J. M., et al. 1993, ApJ, 418, 368
 Goetz, J., Howard, E., Phipper, J., et al. 1999,
<http://astro.pas.rochester.edu/~jagoetz/S88B2/Welcome.html>
 Goetz, J. A., Gutermuth, R., Pipher, J. L., et al. 2003, ApJ, 599, 1173
 Hanson, M. M., Conti, P. S., & Rieke, M. J. 1996, ApJS, 107, 281
 Hartquist, T. W., & Dyson, J. E. 1993, QJRAS, 34, 57
 Henning, Th., Feldt, M., Stecklum, B., et al. 2001, A&A, 370, 100
 Henning, Th., Schreyer, K., Launhardt, R., et al. 2000, A&A, 353, 211
 Henning, Th., & Stecklum, B. 2002, in Modes of Star Formation and The Origin of Field Populations, ed. E. K. Grebel, & W. Brandner, ASP Conf. Ser., 285, 40
 Ho, P. T. P., & Haschick, A. D. 1981, ApJ, 248, 622
 Kasper, M., Looze, D. P., Hippler, S., et al. 2000, Exp. Astron., 10, 49
 Kurtz, S., Churchwell, E., Wood, D. O. S., et al. 1994, ApJS, 26, 907
 Lenzen, R., Bizenberger, P., Salm, N., et al. 1998a, Infrared Astronomical Instrumentation, ed. A. M. Fowler, Proc. SPIE, 3354, 493
 Lenzen, R., Hofmann, R., Bizenberger, P., et al. 1998b, Infrared Astronomical Instrumentation, ed. A. M. Fowler, Proc. SPIE, 3354, 606
 Mezger, P. G., & Henderson, A. P. 1967, ApJ, 147, 471
 Naghizadeh-Khouei, J., & Clarke, D. 1993, A&A, 274, 968
 Okamoto, Y. K., Kataza, H., Yamashita, T., et al. 2003, ApJ, 584, 368
 Phillips, J. P., & Mampaso, A. 1991, A&AS, 88, 189
 Pratap, P., Megeath, S. T., & Bergin, E. A. 1999, ApJ, 517, 799
 Rousset, G., Lacombe, F., Puget, P., et al. 2000, Adaptive Optical Systems Technology, ed. P. L. Wizinowich, Proc. SPIE, 4007, 72
 Rudolph, A., Welch, W. J., Palmer, P., et al. 1990, ApJ, 363, 528
 Schaefer, D., de Koter, A., Schmutz, W., et al. 1996, A&A, 312, 475
 Schwartz, P. R., Wilson, W. J., & Epstein, E. E. 1973, ApJ, 186, 529
 Serkowski, K. 1958, Acta Astron., 8, 135
 Serkowski, K. 1962, Advances in Astronomy and Astrophysics, ed. Z. Kopal (Academic Press), 1, 289
 Simmons, J. F. L., & Stewart, B. G. 1985, A&A, 142, 100
 Simpson, J. P., & Rubin, R. H. 1990, ApJ, 354, 165
 Smith, L. J., & Norris, R. P. F., & Crowther, P. A. 2002, MNRAS, 337, 1309
 Vacca, W. D., Garmany, C. D., & Shull, J. M. 1996, ApJ, 460, 914
 Wardle, J. F. C., & Kronberg, P. P. 1974, ApJ, 194, 249
 Watson, A. M., & Hanson, M. M. 1997, ApJ, 490, L165
 Wegner, W. 1994, MNRAS, 270, 229
 Weintraub, D. A., Kastner, J. H., & Mahesh, A. 1994, ApJ, 420, L87
 Weintraub, D. A., & Kastner, J. 1993, ApJ, 411, 767
 Welch, W. J., Dreher, J. W., Jackson, J. M., et al. 1987, Science, 238, 1550
 White, G. J., & Fridlund, C. V. M. 1992, A&A, 266, 452
 Whittet, D. C. B., Martin, P. G., Hough, J. H., et al. 1992, ApJ, 386, 562
 Wood, D. O. S., & Churchwell, E. 1989, ApJS, 69, 831
 Yorke, H. W., Tenorio-Tagle, G., & Bodenheimer, P. 1983, A&A, 127, 313
 Zickgraf, F. J., Wolf, B., Leitherer, C., et al. 1986, A&A, 163, 119